Sensors & Actuators: B. Chemical 321 (2020) 128527

Contents lists available at ScienceDirect

Sensors and Actuators B: Chemical

journal homepage: www.elsevier.com/locate/snb

Ultrasensitive detection of bisphenol A under diverse environments with an electrochemical aptasensor based on multicomponent AgMo heteronanostructure

Yingpan Song, Miaoran Xu, Zhenzhen Li, Lina He, Mengyao Hu, Linghao He, Zhihong Zhang*, Miao Du*

College of Material and Chemical Engineering, Zhengzhou University of Light Industry, Zhengzhou 450001, PR China

ARTICLE INFO

Keywords:
Ag(I) polyoxometalate
Molybdenum disulfide
Multicomponent nanohybrid
Impedimetric aptasensor
Detection of bisphenol A

ABSTRACT

A novel series of bimetallic AgMo heteronanostructures (Ag-PMo_{12}) were prepared by annealing silver ions doped phosphomolybdic acid ($H_3PMo_{12}O_{40}$) at different temperatures (300, 600, and 800 °C), and explored as the sensitive platforms for developing electrochemical biosensors to detect the trace bisphenol A (BPA). Amongst, Ag-PMo_{12} calcinated at 600 °C gave a multicomponent nanohybrid of Ag, Ag_2O, Ag_2S, and ultra-thin MoS_2 nanosheet (denoted as $Ag/Ag_2O/Ag_2S/MoS_{2(600)}$). This nanohybrid exhibited active electrochemical performance, excellent biocompatibility, strong bioaffinity and superior adsorbability to aptamer strands, leading to optimal sensing performance in comparison with other hybrids. As a result, the $Ag/Ag_2O/Ag_2S/MoS_{2(600)}$-based aptasensor displayed an ultralow detection limit of 0.2 fg mL^{-1} within the BPA concentration of 1–1000 fg mL^{-1}. This aptasensor also showed high selectivity and good stability, reproducibility, regenerability, and applicability in different situations. This result will not only develop an excellent sensing platform toward BPA detection in aspects of environmental monitoring, food safety, and human health, but also present a promising sensing strategy that can be extensively explored to detect other targets via anchoring of various aptamer strands.

1. Introduction

Bisphenol A (BPA) has been produced in high volume and widely applied in chemical industry. BPA can be found in various products, such as baby bottles, beverage containers, medical equipment, food packaging, and thermal papers, and its global consumption in 2016 was 8 million metric tons, leading to a wide contamination in different environments [1]. The European Union has mandated that the BPA amount in products should be less than 3 mg kg^{-1}. Since 2011, its utilization in baby bottle production was prohibited in China because BPA with low dosage can result in endocrine dyscrasia and tumors [2]. Due to the negative effects of BPA on the environment and human health, the detection of trace BPA is urgently needed in order to enhance the food safety, monitor the environment, and improve the human health. Currently, several methods, such as enzyme-linked immunosorbent assay [3], surface enhanced Raman scattering (SERS) [4], surface plasmon resonance [5], quartz crystal microbalance [6], fluorescence [7], and electrical sensing [8] have been developed to detect BPA. In this regard, electrochemical biosensors have received increasing attention for the fast response and feasible operation [9]. Different probe molecules, including enzymes [10], antibodies [11], and aptamers [12], can serve as the bio-recognition elements to achieve the high selectivity of electrochemical biosensors. Notably, aptamers have been most widely applied owing to their high stability, easy modification, repeatable and simple synthesis, and low cost [8].

To improve the detection sensitivity of electrochemical biosensors, diverse types of electrode materials, including carbon materials, inorganic nanoparticles, and porous organic frameworks, have been explored [13]. Amongst, molybdenum chalcogenides have attracted much attention for their low toxicity in sensing organic analytes, high surface activity, and tailorable surface/electronic structures [14], thus illustrating promising biosensing performances for the determination of heavy metal ions [15], H_2O_2 for cancer cells [16], or miRNA [17]. Particularly, MoS_2, a layered transition metal dichalcogenides, have aroused a lot of interests for biosensors [18] due to its inexpensive price, good stability [19], and potential catalytic properties [20,21]. For instance, biofunctionalized MoS_2 nanosheet was used as fluorescent probe for in situ detecting targeted miRNA in living cancer cells, in

* Corresponding authors.
E-mail addresses: 2006025@zzuli.edu.cn (Z. Zhang), dumiao@zzuli.edu.cn (M. Du).

https://doi.org/10.1016/j.snb.2020.128527
Received 7 February 2020; Received in revised form 26 May 2020; Accepted 26 June 2020
Available online 28 June 2020
0925-4005/

which MoS_2 nanosheet offered advantages of high fluorescence quenching efficiency and extremely low toxicity [22]. Chemical vapor deposition-grown monolayer MoS_2 films were adopted for the construction of field-effect transistor-based DNA biosensor and explored for noninvasive prenatal testing of trisomy 21 syndrome, which can reliably detect target DNA fragments (chromosome 21 or 13) with a detection limit below 100 aM [23]. Unfortunately, the relatively lower electrical conductivity of MoS_2 (1.56×10^{-4} S cm^{-1}) serves as a barrier in electrochemical sensing [24]. This shortcoming of MoS_2 can be solved by introducing conductive metal nanoparticles (Au, Ag, and Cu) for the formation of multi-metallic heterostructure [25,26]. Furthermore, the MoS_2 nanosheets were also obtained by the hydrothermal strategy using an Anderson-type $(NH_4)_4[M_{II}Mo_6O_{24}H_6]\cdot 6H_2O$ polyoxometalates (M = Co, Ni, Fe) as bimetal precursors and thiourea as modifier [27–29]. Integrating with other metal ions, this multiple metallic doped MoS_2 architecture demonstrates a disordered structure, exposure of active heterointerfaces, a "highway" of charge transport on two dimensional conductive channels, and abundant active catalytic sites from the synergistic effect of the heterostructures, thus showing outstanding applicability in electrochemical catalysts and biosensors [30,31].

Among these metals, Ag has been a key focus of the research and development to construct biosensors owing to the convenient synthesis, ultrasmall size, excellent conductivity, catalytic activity, biocompatibility, cell viability, and environmentally responsive properties [32]. Recently, Ag-polyoxometalates (Ag-POM) hybrids or nanocomposites were prepared and mainly applied for catalytic and photocatalytic [33–35]. For example, a Keggin type polyoxometalate, $[PMo_{12}O_{40}]^{3-}$ (PMo_{12}) was mixed with $AgNO_3$ to obtain Ag-PMo nanocomposite by electrodeposition, in which metallic Ag was formed upon reduction of Ag^+. In this way, the adsorption of PMo_{12} on the surface of the newly formed Ag lowered its surface energy and stabilized the nanostructure, thus improving the electrocatalytic performance of the Ag-PMo_{12} nanocomposite for CO_2 reduction [36]. Similarly, a typical $\{Ag_6Mo_7O_{24}\}$ @Ag-MOF provided more active sites, faster ion/electron transfer, and electrolyte diffusion pathways, resulting in excellent specific capacitance higher than other compounds. These investigations further proved the high electrocatalytic activity of AgMo heterostructure [37]. According to these above discussions, it would be high desirable for the development of the bimetallic AgMo heteronanostructure based on Ag-POM and exploring it as the platforms for anchoring aptamer strands to construct biosensor. Nevertheless, the investigation of POM-derivatives based electrochemical aptasensors is still in its infancy, especially those for detecting small hazardous molecules in polluted environments or foods.

In this work, silver doped phosphomolybdic acid was prepared by hydrothermal method using phosphomolybdic acid $H_3PMo_{12}O_{40}$ (PMo_{12}), $AgNO_3$, and thioacetamide (CH_3CSNH_2) as raw materials (denoted as Ag-PMo_{12}). Novel electrochemical aptasensors were constructed for the determination of BPA based on the bimetallic AgMo heteronanostructures obtained by annealing Ag-PMo_{12} at different temperatures of 300, 600, and 800 °C (Scheme 1). Firstly, MoS_2 nanosheets were produced by the reaction of PMo_{12} and CH_3CSNH_2 [29] and doped with abundant Ag^+ ions by the hydrothermal method. During the calcination at high temperature, most of Ag^+ ions were oxidized to Ag_2O and vulcanized to Ag_2S, where small amount of Ag^+ ions were reduced to Ag^0 nanoparticles when calcined at extremely high temperature (600 and 800 °C) [38]. Due to the strong bioaffinity between DNA strands and MoS_2 [39,40] or Ag-based substances [41], abundant BPA aptamer can anchor over the Ag/Ag_2O/Ag_2S/MoS_2 matrix in virtue of $\pi-\pi$ stacking interaction [42], Van Der Waals force [43], and coordination interaction between metal oxide or sulfide and DNA aptamer strands [44], leading to a superior sensing performance for BPA. In comparison with the aptasensors on the basis of PMo_{12}, Ag-PMo_{12}, Ag-$MoS_{2(300)}$, and Ag/Ag_2O/Ag_2S/$MoS_{2(800)}$, the Ag/Ag_2O/Ag_2S/$MoS_{2(600)}$ nanohybrid-based aptasensor showed remarkably high detection sensitivity due to its excellent electrochemical activity, large specific surface area, good biocompatibility, and homogeneous multiphases. Further, compared with the known BPA sensors, the Ag/Ag_2O/Ag_2S/$MoS_{2(600)}$-based aptasensor illustrated the following advantages: (i) simple material preparation using hydrothermal method and calcination process without any post-synthesis, (ii) label-free aptamer strands without electrochemical indicators, and (iii) great enhancement of the electrochemical signal by active Ag and Mo centers [36,37]. This sensing strategy also establishes a new platform for different aptasensors towards environmental monitoring and food safety.

2. Materials and methods

The sections of materials and chemicals, synthesis of PMo_{12} nanosheets (NSs), preparation of all solutions, pretreatment of bare Au electrode (AE), basic characterizations, and electrochemical measurements, was supplied in Supplementary Material (S1 part).

2.1. Synthesis of Ag-PMo_{12} and the series of Ag-PMo_{12}-derived nanohybrids

PMo_{12} NSs were prepared as described in S1.2 (Supplementary Material). The preparation of Ag-PMo_{12} was similar to that of PMo_{12}, except for the addition of $AgNO_3$ solution (by dissolving 1 g of $AgNO_3$ into 10 mL of Milli-Q water).

A series of Ag-PMo_{12}-derived nanohybrids were obtained from Ag-PMo_{12} via annealing at different temperatures (300, 600, and 800 °C). First, Ag-PMo_{12} (100 mg) was transferred into a tube furnace and heated at 300, 600 and 800 °C, respectively, under N_2 atmosphere for 2 h at a heating rate of 5 °C min^{-1}. The calcined sample was collected after cooling to room temperature under N_2. The final products were denoted as Ag-$MoS_{2(300)}$, Ag/Ag_2O/Ag_2S/$MoS_{2(600)}$, and Ag/Ag_2O/Ag_2S/$MoS_{2(800)}$ based on their components and calcination temperatures. Besides, the usage of N_2 atmosphere was to maintain the whole calcination process in an oxygen-free environment to avoid that the sample reacted with the oxygen in air. During the annealing process, $H_3PMo_{12}O_{40}$ was reacted with CH_3CSNH_2 and transformed to MoS_2, while Ag^+ ions were transformed to Ag_2O, Ag_2S, or Ag^0. Actually, it is pretty hard for nitrogen to react with the sample. Consequently, no compound containing N was found in XRD and XPS.

2.2. Fabrication of aptasensors based on different nanomaterials

Five types of aptasensors on the basis of different electrode materials such as PMo_{12}, Ag-PMo_{12}, Ag-$MoS_{2(300)}$, Ag/Ag_2O/Ag_2S/$MoS_{2(600)}$, and Ag/Ag_2O/Ag_2S/$MoS_{2(800)}$ were developed for BPA detection. The optimal electrode material was used for further electrochemical tests after comparing the sensing performances of aptasensors. As an example, the fabrication procedure of the Ag/Ag_2O/Ag_2S/$MoS_{2(600)}$-based aptasensor was described below in detail. The Ag/Ag_2O/Ag_2S/$MoS_{2(600)}$ powder (1.0 mg) was dispersed into Milli-Q water (1.0 mL) and fully mixed by ultra-sonication to obtain a homogeneous Ag/Ag_2O/Ag_2S/$MoS_{2(600)}$ suspension. Then, the Ag/Ag_2O/Ag_2S/$MoS_{2(600)}$ suspension (5.0 μL, 1.0 mg mL^{-1}) was dropped onto the pretreated AE surface and dried at room temperature for 3 h to obtain Ag/Ag_2O/Ag_2S/$MoS_{2(600)}$/AE, which was separately rinsed by ethanol and Milli-Q water. Afterward, the modified AE was incubated with the aptamer solution (100 nM) at 4 °C for 30 min for ensuring the saturated anchoring of aptamer over the Ag/Ag_2O/Ag_2S/$MoS_{2(600)}$/AE surface. Finally, the as-prepared Apt/Ag/Ag_2O/Ag_2S/$MoS_{2(600)}$/AE was immersed in BPA solution for further electrochemical measurements (denoted as BPA/Apt/Ag/Ag_2O/Ag_2S/$MoS_{2(600)}$/AE).

2.3. Electrochemical measurements

The detail for electrochemical measurements was listed in S1.6 (Supplementary Material). The BPA detection was explored by both

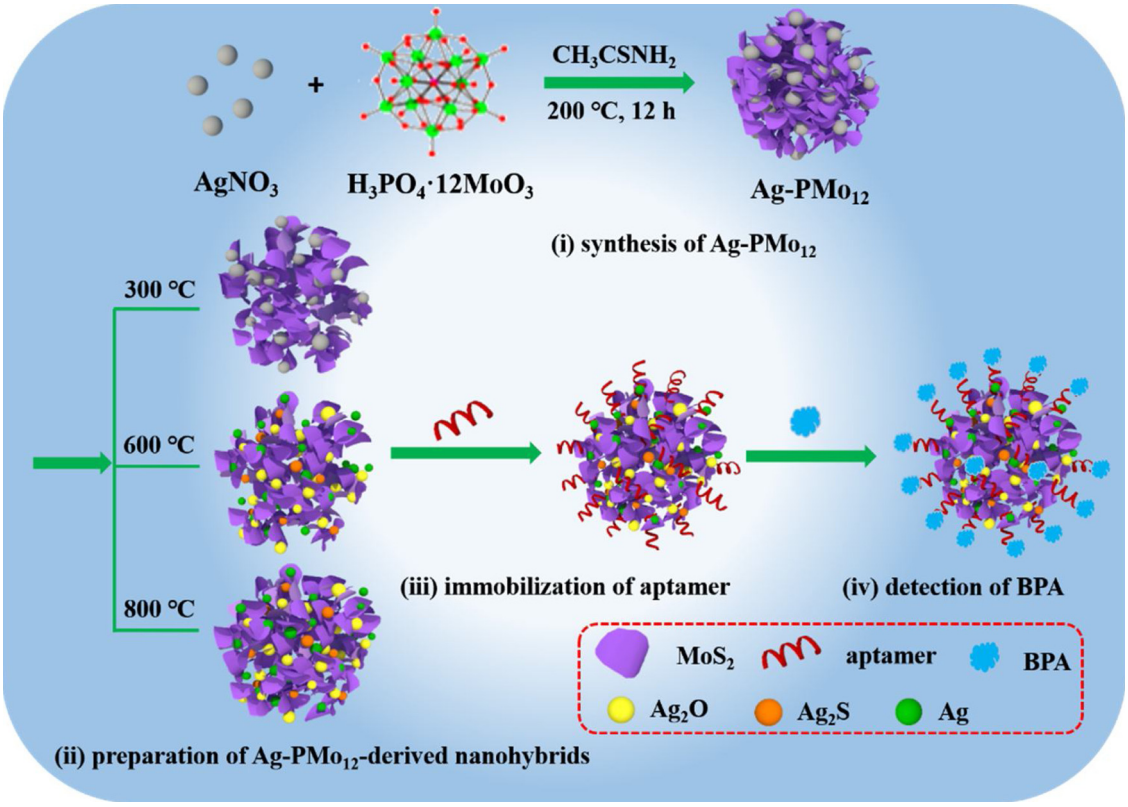

Scheme 1. Fabrication procedure of the Ag-PMo_{12}-derived nanohybrids-based aptasensors for BPA detection, including (i) synthesis of Ag-PMo_{12}, (ii) preparation of Ag-PMo_{12}-derived nanohybrids, (iii) immobilization of aptamer, and (iv) detection of BPA.

cyclic voltammetry (CV) and electrochemical impedance spectroscopy (EIS) techniques using different aptasensors based on PMo_{12}, Ag-PMo_{12}, and the series of Ag-PMo_{12}-derived nanohybrids.

To obtain the optimal experimental conditions, different parameters such as the dosage of the chosen nanohybrid, the aptamer concentration, and the binding time of BPA with the aptasensor were optimized for detecting BPA. Herein, different dosages of the chosen nanohybrid (0.1, 0.2, 0.5, 1, and 2 mg mL^{-1}) were applied to evaluate the sensing performance of aptasensor for the detection of BPA. Moreover, the modified AEs were incubated with the aptamer solutions with different concentrations (10, 20, 50, 100, 200, and 500 nM) to optimize the experimental condition for achieving the highest detection efficiency for BPA. Also, the aptasensor was incubated with BPA solution and recorded by EIS at diverse durations to obtain the influence of binding time on the sensing performance. As such, the optimal experimental conditions can be determined for further measurements.

The detection limit of aptasensor was assessed by incubating Apt/Ag/Ag_2O/Ag_2S/MoS_2/AE with different concentrations of BPA solution (0.001, 0.005, 0.01, 0.05, 0.1, 0.5, and 1 pg mL^{-1}) and recorded with EIS, followed by fitting all EIS Nyquist plots using the Zview2 software.

The reproducibility was explored by developing five aptasensors independently and assessed by EIS for comparing their sensing performances. The stability of aptasensor was characterized by storing BPA/Apt/Ag/Ag_2O/Ag_2S/MoS_2/AE in refrigerator (4 °C) for 15 days and determined by EIS every day.

For probing the selectivity of aptasensor, the Apt/Ag/Ag_2O/Ag_2S/MoS_2/AE was immersed with the interferences including uric acid (UA), benzidine (DAB), phenol (PN), 4-nitrophenpl (NPN), dopamine (DA), ascorbic acid (AA), benzaldehyde (BA), benzophenone (BP), resorcinol (DB), and their mixture with BPA, and studied by EIS. In each case, the concentration of interference (1 ng mL^{-1}) is 100-folds that of BPA.

The regenerability of aptasensor was obtained by rinsing BPA/Apt/Ag/Ag_2O/Ag_2S/MoS_2/AE using 1 mM NaOH at room temperature for 5 min, and followed by rinsing with a large amount of phosphate buffer solution (PBS). Then, the electrode was immersed into BPA solution (1 fg mL^{-1}) until the EIS response was up to the origin level. The same procedure was repeated by 7 cycles.

2.4. Real sample analysis

River water, milk and human serum were used to assess the applicability of aptasensor. The river water was taken from the Xushui River at the High-tech Zone in Zhengzhou, China. Milk was from Yonghui supermarket in Zhengzhou, China. Human serum was purchased from Beijing Solarbio Science & Technology Co., Ltd. A 3 kDa dialysis bag was used to remove the interfered compounds from human serum, allowing BPA with low molecular weight to pass through. The BPA solutions with different concentrations (0.001, 0.005, 0.01, 0.05, 0.1, 0.5, and 1 pg mL^{-1}) were added into the three types of samples to test the applicability. The incubation time of aptasensor with the real samples was 30 min.

3. Results and discussion

3.1. Chemical structures/components of Ag-PMo_{12} and the series of Ag-PMo_{12}-derived nanohybrids

The basic characterizations of PMo_{12} NSs and Ag-PMo_{12} were provided and discussed in S2 (Supplementary Material). Their Field emission scanning electron microscope (FE-SEM) and Transmission electron microscopy (TEM) images (Figs. S2 and S3) showed that MoS_2 NSs was derived from PMo_{12} by the hydrothermal method. Further, FE-SEM images (Figs. S3a and b) of Ag-PMo_{12} showed a tight and large sphere-shape. The solid block sphere in TEM image (Fig. S3c) hinted its dense structure. HR-TEM image suggested that the dense spheres are

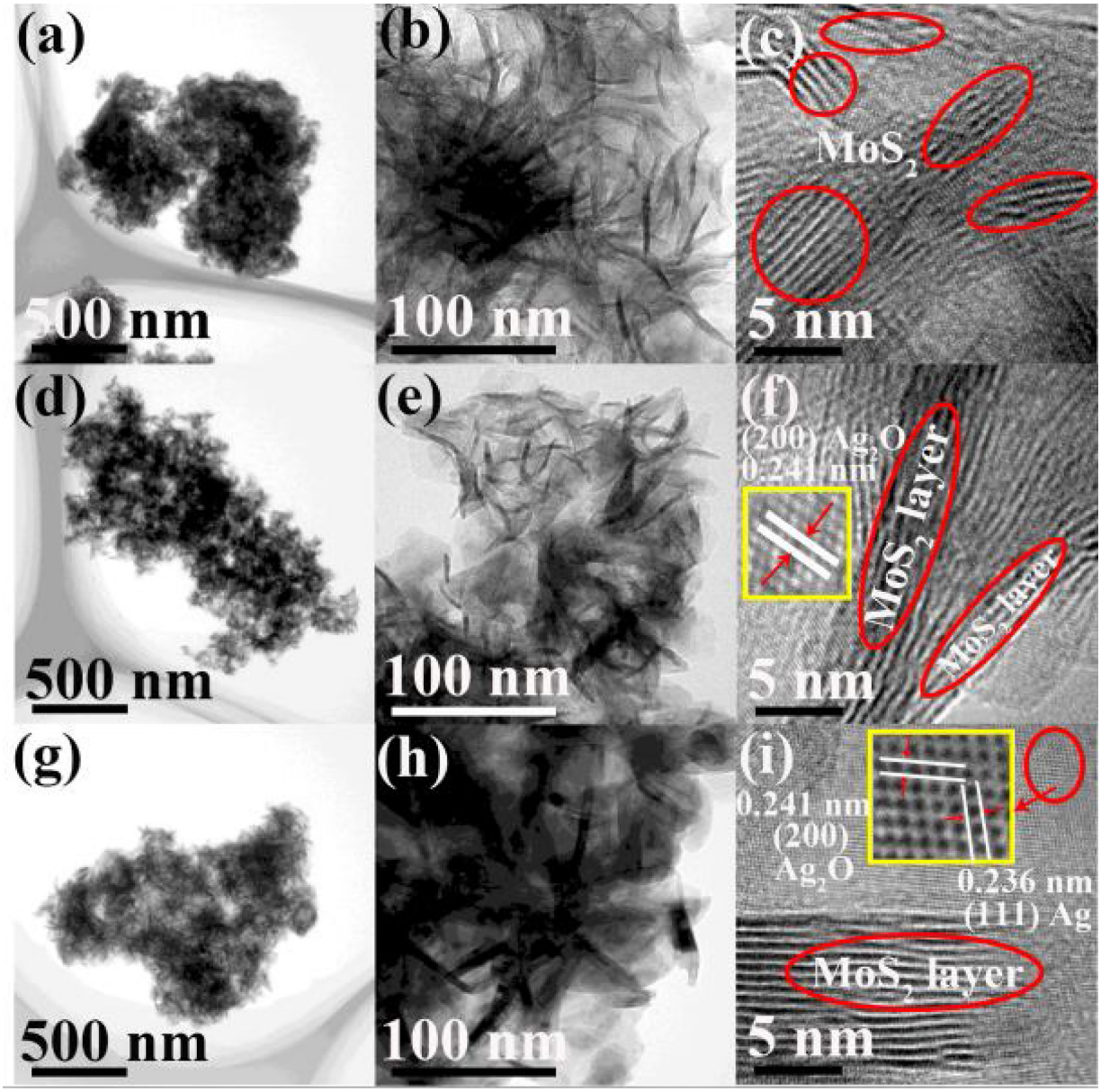

Fig. 1. TEM and HR-TEM images of (a, b, c) Ag-$MoS_{2(300)}$, (d, e, f) $Ag/Ag_2O/Ag_2S/MoS_{2(600)}$, and (g, h, i) $Ag/Ag_2O/Ag_2S/MoS_{2(800)}$.

wrapped by thin layers (Fig. S3d), also showing the lattice spacing of MoS_2 NSs (Fig. S3e). No Ag-related lattice was observed, indicating its ionic state doped in the MoS_2 NSs.

Figs. S4 and 1 indicated the FE-SEM and HR-TEM images of the series of Ag-PMo_{12}-derived nanohybrids. The surface morphologies of Ag-$MoS_{2(300)}$ and $Ag/Ag_2O/Ag_2S/MoS_{2(800)}$ were similar with that of the PMo_{12} spheres with irregular shape (Figs. S4a, b, e, and f). However, irregular flowers were observed for the $Ag/Ag_2O/Ag_2S/MoS_{2(600)}$ nanohybrid (Figs. S4c and d), composed of a number of nanosheets with loose nanostructure. Although the nanosheet structure was obscurely found for Ag-$MoS_{2(300)}$ and $Ag/Ag_2O/Ag_2S/MoS_{2(800)}$, their TEM images obviously showed the assembled nanosheets (Fig. 1a, b, g and h), which were similar to the $Ag/Ag_2O/Ag_2S/MoS_{2(600)}$ nanohybrid (Fig. 1d and e). Among the three samples, the $Ag/Ag_2O/Ag_2S/MoS_{2(600)}$ nanohybrid showed the looser structure and thinner nanosheets, which was consistent with the FE-SEM results. The HR-TEM images (Fig. 1c, f, and i) indicated lattice spacing of the (002) plane of MoS_2 [45]. An additional lattice spacing of 0.241 nm appeared in $Ag/Ag_2O/Ag_2S/MoS_{2(600)}$, owing to the (200) plane of Ag_2O [46]. With regard to $Ag/Ag_2O/Ag_2S/MoS_{2(800)}$, another new lattice spacing of 0.236 nm assigned to the (111) plane of metal Ag [47] is observed apart from Ag_2O and MoS_2 in the HR-TEM image (Fig. 1i). These results revealed the Ag^+ ions doped in PMo_{12} was not transferred after annealing at 300 °C, but showing the preferable oxidation state of Ag_2O when the calcination temperature was higher than 600 °C. When the annealing temperature was further increased, partial Ag component was reduced to the metal state, Ag.

The crystal structures were studied by X-ray diffraction (XRD). The XRD pattern of PMo_{12} (Fig. 2a) showed three diffraction peaks at 8.9°, 33.4°, and 58.3° from MoS_2 [48], which was confirmed by the HR-TEM result. In this work, MoS_2 was produced when PMo_{12} was treated with CH_3CSNH_2 by hydrothermal method. However, no obvious peak was observed in Ag-PMo_{12} due to its low crystallization. As for Ag-$MoS_{2(300)}$, three characteristic peaks appeared at 13.9°, 33.4°, and 58.3°, which was ascribed to MoS_2 [48]. This result demonstrated that, when the temperature was low, PMo_{12} contained in Ag-PMo_{12} transformed to MoS_2, while Ag^+ ions doped in Ag-PMo_{12} still kept their ionic state, and had no effect on the XRD patterns of Ag-$MoS_{2(300)}$. The XRD

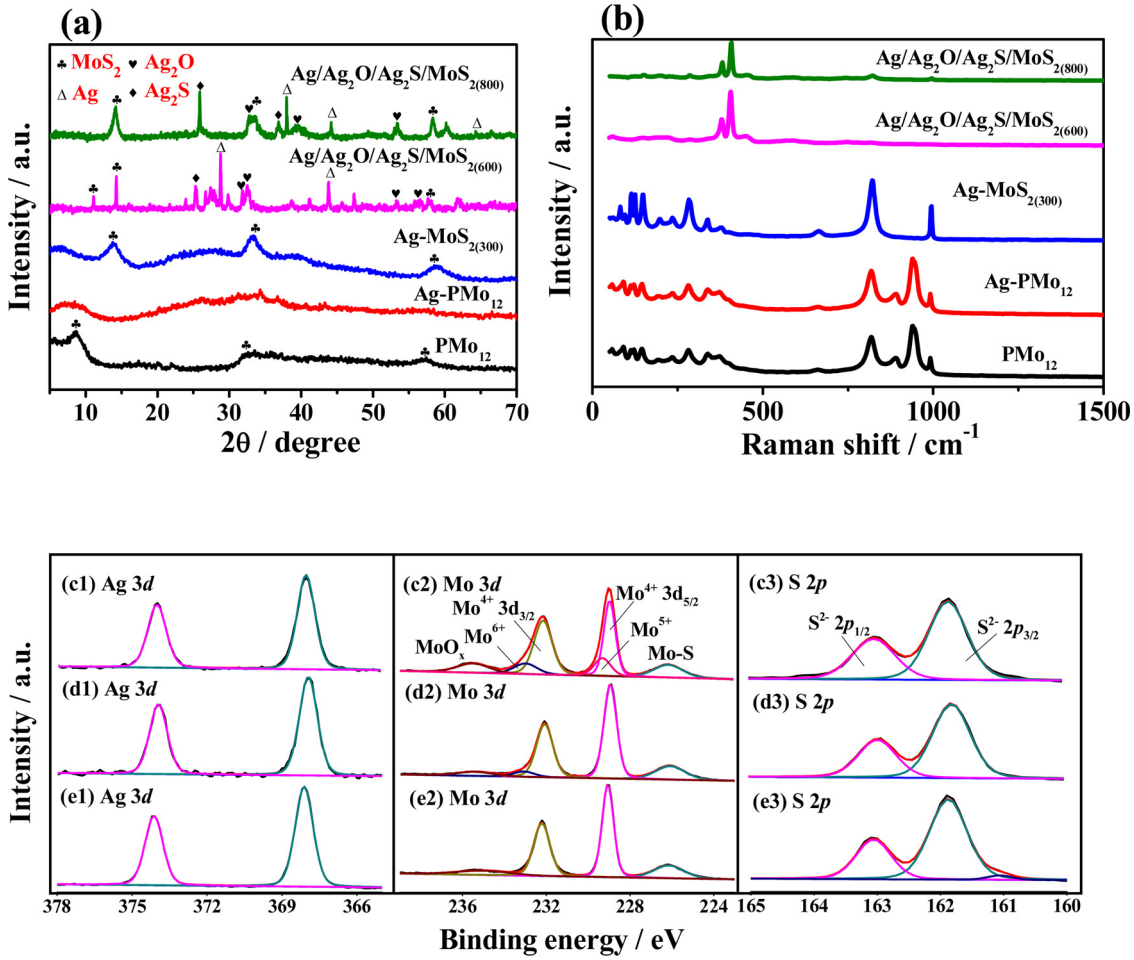

Fig. 2. (a) XRD patterns and (b) Raman spectra of PMo_{12}, Ag-PMo_{12}, and the three nanohybrids. High-resolution (c1, d1, e1) Ag 3*d*, (c2, d2, e2) Mo 3*d*, and (c3, d3, e3) S 2*p* XPS spectra of (c) Ag-$MoS_{2(300)}$, (d) $Ag/Ag_2O/Ag_2S/MoS_{2(600)}$, and (e) $Ag/Ag_2O/Ag_2S/MoS_{2(800)}$.

pattern of $Ag/Ag_2O/Ag_2S/MoS_{2(600)}$ indicates the characteristic peaks at 11.2°, 13.9°, 33.4°, and 58.3° due to MoS_2 [48] as well as the peaks at 32.0°, 32.6°, 53.3°, and 56.5° attributed to Ag_2O [49]. Two other peaks at 25.4° and 45.6° are assigned to Ag_2S; while the peaks at 28.9°, 38.5°, and 44.1° are ascribed to metal Ag [50]. Apparently, when the calcination temperature increased to 600 °C, the reactions of Ag^+ ions with $(PMo_{12}O_{40})^{3-}$ and S^{2-} occurred, resulting in the formation of Ag_2O/Ag_2S nanocrystals, which were embedded within the MoS_2 nanosheets. Besides, a small partial Ag^+ ions were reduced to its metallic state, Ag^0. As such, the MoS_2 nanosheets were utilized as the support of Ag_2S, Ag_2O, and Ag^0 nanocrystals, which can avoid them to be aggregated and greatly improve the electrochemical activity and bioaffinity toward aptamer [20]. That is to say, the $Ag/Ag_2O/Ag_2S/MoS_{2(600)}$ nanohybrid is comprised of multiple components. The XRD pattern of $Ag/Ag_2O/Ag_2S/MoS_{2(800)}$ illustrates similar composition as that of $Ag/Ag_2O/Ag_2S/MoS_{2(600)}$. However, the formed O/S-related gas molecules were released at 800 ℃ [44], leading to more Ag^+ ions reduced to Ag^0. These results suggest that Ag-PMo_{12} was changed to MoS_2 NSs embedded with multiple components of Ag_2O, Ag_2S, and Ag^0 in the presence of CH_3CSNH_2 by annealing at extremely high temperatures. Obviously, the component and structure of the products were remarkably affected by the calcination temperature. This conversion in the chemical structure and components of Ag-PMo_{12} can remarkably enhance the electrochemical activity and facilitate the biomolecule adsorption. As discussed in the previously reported work [41], the high-resolution XPS spectra revealed that Ag atoms mainly interact with oxygen atoms of the phosphodiester bond and deoxyribose bearing on DNA, while the Ag^+ ions preferentially interact with the nitrogen atoms of the DNA bases. Therefore, different valence states of Ag components can lead to different combination modes with DNA, further resulting in different adsorption capacity of the three nanohybrids. As shown in XRD patterns, Ag-$MoS_{2(300)}$ includes one existence form of Ag^+, and can only interact with the nitrogen atoms on DNA bases. Since $Ag/Ag_2O/Ag_2S/MoS_{2(600)}$ includes Ag_2O, Ag_2S and Ag^0, it can interact both with nitrogen atoms on DNA bases and oxygen atoms of the phosphodiester bond and deoxyribose in DNA. Even the $Ag/Ag_2O/Ag_2S/MoS_{2(800)}$ hybrid has the similar composition with that of $Ag/Ag_2O/Ag_2S/MoS_{2(600)}$, the high crystallinity and regular nanostructure of $Ag/Ag_2O/Ag_2S/MoS_{2(800)}$ are unfavorable for anchoring aptamer strands. By comparison, their electrochemical activities and biomolecule adsorption follow the order of $Ag/Ag_2O/Ag_2S/MoS_{2(600)}$ > Ag-$MoS_{2(300)}$ > $Ag/Ag_2O/Ag_2S/MoS_{2(800)}$, which is also verified by their electrochemical results (Fig. 3d).

Raman spectroscopy was also used to investigate their chemical structures. The Raman spectrum of PMo_{12} (Fig. 2b) revealed the specific peaks located at 281, 378, 405, 818, and 942 cm^{-1}, which were attributed to the E^1_{2g} and A_{1g} vibrational modes of MoS_2 [51]. The Raman spectrum of Ag-PMo_{12} is the same as that of PMo_{12}. This result revealed that the addition of Ag^+ has no influence on the chemical structure of PMo_{12}. Those main peaks originating from MoS_2 are also observed for Ag-$MoS_{2(300)}$ after annealing at 300 °C, indicating that the chemical structure of Ag-PMo_{12} was slightly changed. However, only two MoS_2 bands at 378 and 405 cm^{-1} are found for $Ag/Ag_2O/Ag_2S/MoS_{2(600)}$ and $Ag/Ag_2O/Ag_2S/MoS_{2(800)}$. Compared with the Raman modes of PMo_{12}, the E^1_{2g} mode of $Ag/Ag_2O/Ag_2S/MoS_{2(600)}$ and $Ag/Ag_2O/Ag_2S/MoS_{2(800)}$ nanohybrids obviously upshifted as a result of the softening

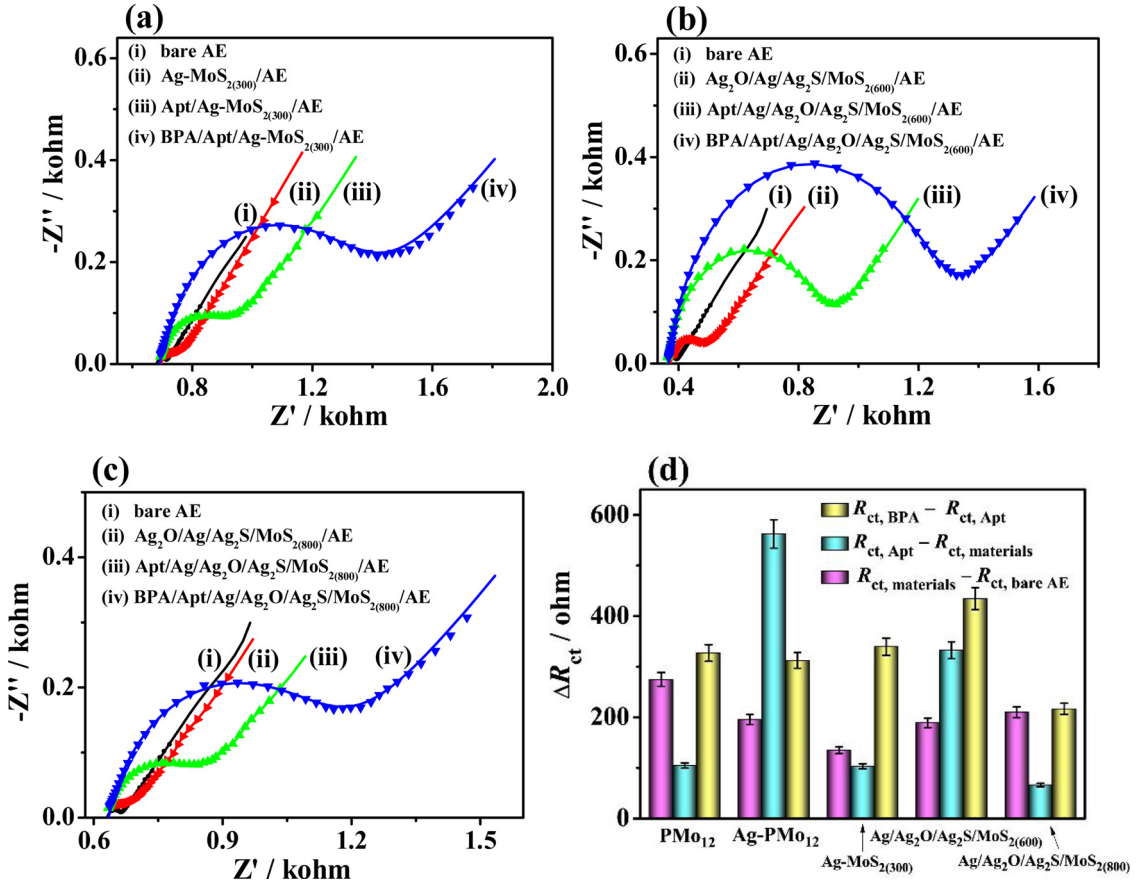

Fig. 3. EIS Nyquist plots of the aptasensors based on (a) Ag-$MoS_{2(300)}$, (b) Ag/Ag_2O/Ag_2S/$MoS_{2(600)}$, and (c) Ag/Ag_2O/Ag_2S/$MoS_{2(800)}$ for detecting BPA in PBS containing 5.0 mM $[Fe(CN)_6]^{3-/4-}$ redox probe. (d) Variations in R_{ct} for each stage during the fabrication procedure of BPA aptasensors based on PMo_{12}, Ag-PMo_{12}, Ag-$MoS_{2(300)}$, Ag/Ag_2O/Ag_2S/$MoS_{2(600)}$, and Ag/Ag_2O/Ag_2S/$MoS_{2(800)}$.

of E^1_{2g} vibrations, suggesting that the interaction between Ag/Ag_2O/Ag_2S and MoS_2 obviously softened the lateral vibration between S and Mo atoms [20].

Fig. S5 shows the N_2 adsorption and desorption isotherms of the five samples. The specific surface areas are 93.6, 151.3, 138.5, 19.5, and 23.8 $m^2 g^{-1}$, respectively, for PMo_{12}, Ag-PMo_{12}, Ag-$MoS_{2(300)}$, Ag/Ag_2O/Ag_2S/$MoS_{2(600)}$, and Ag/Ag_2O/Ag_2S/$MoS_{2(800)}$, with the pore sizes of 18.6–95.1, 18.6–94.7, 3.6–11.4, 3.7–5.3/6.2–29.1, and 3.8–5.4/6.0–31.1 nm, revealing their mesoporous features. PMo_{12} and Ag-PMo_{12} show larger pore sizes, while after calcination of Ag-PMo_{12}, the coordination effect between Ag^+ and PMo_{12} can be weaken, and the formed Ag/Ag_2O/Ag_2S nanocrystals are possibly to embed within the MoS_2 nanosheets, leading to a great decrease of pore size. Despite this, the high mesoporosity of Ag/Ag_2O/Ag_2S/MoS_2 still endows them with excellent electrochemical activity. These features are favorable for the enhancement of biosensing performance of the Ag/Ag_2O/Ag_2S/MoS_2-based aptasensors.

The high-resolution X-ray photoelectron spectroscopy (XPS) for each element containing in PMo_{12} and Ag-PMo_{12} was analyzed and shown in Supplementary Material (S2 part). The results verify that PMo_{12} and Ag-PMo_{12} comprise the mixed valences of Mo (Mo^{4+}/Mo^{5+}/Mo^{6+}) and S (S^{2-}/S_2^{2-}/S^{6+}), multiple Mo—O/Mo—S/S—O/C—O components, and abundant oxygen vacancies, which can remarkably facilitate the electron transfer and improve the electrochemical activity [52]. Moreover, a clear Ag^+ signal is observed in Ag-PMo_{12}.

As for the series of Ag-PMo_{12}-derived nanohybrids (Fig. 2c–e), the high-resolution Ag 3*d* XPS spectra also demonstrate two clear peaks, which are ascribed to Ag^+ and similar to those of Ag-PMo_{12}. The Mo 3*d* XPS spectrum of Ag-$MoS_{2(300)}$ shows a relative high content of Mo^{5+} and Mo^{6+} ions among the three samples and Mo—O_x bond is observed. By contrast, the Mo^{6+} ion containing in Ag/Ag_2O/Ag_2S/$MoS_{2(600)}$ displays a low intensity because of its small peak area [53]. For Ag/Ag_2O/Ag_2S/$MoS_{2(800)}$, only low content of Mo—O_x bond is found without any Mo^{5+}/Mo^{6+} ion, indicating its complete decomposition at higher temperature. The large peak area of Mo^{4+} ion (Figs. 2d2 and e2) further demonstrated that most of the Mo^{5+}/Mo^{6+} ions were reduced to Mo^{4+} ion by the hydrothermal method, and MoS_2 was produced during this process. Only S^{2-} $2p_{3/2}$ and S^{2-} $2p_{1/2}$ peaks appear in the S 2*p* XPS spectra for the series of nanohybrids, suggesting the production of Ag_2S or MoS_2. The above analysis indicates that calcination of Ag-PMo_{12} at high temperatures results in nanohybrid products containing Ag, Ag_2O, Ag_2S, and MoS_2, with ultra-thin nanosheet structure, mixed chemical valence, multiple components, and abundant oxygen vacancies. These features could not only boost the electron transfer but also improve the biomolecule anchoring [54], which thus enhance the sensing performance of the electrochemical aptasensor.

3.2. Electrochemical sensing performance of the aptasensors based on the samples

Herein, the EIS and CV approaches have been applied to verify the fabrication procedure of the aptasensors based on PMo_{12}, Ag-PMo_{12}, and the series of Ag-PMo_{12}-derived nanohybrids. Figs. S9 and S10 present the CV curves for BPA detection by different aptasensors. The bare AEs show typical well-defined redox peaks with a high peak current of 200.3 μA, along with the narrow peak-to-peak separation (ΔE_p) of 0.17 V. The high peak current and narrow ΔE_p reveal the excellent electrochemical activity of the bare AE. After modification with different nanomaterials, the peak current of the modified AE clearly

declines, accompanied with the increase of ΔE_p. Among these electrode materials, $Ag/Ag_2O/Ag_2S/MoS_{2(600)}$/AE shows the highest peak current and narrowest ΔE_p value, indicating its good electrochemical performance. This results also demonstrates that the annealing treatment of Ag-PMo_{12} at appropriate temperature is beneficial for accelerating the electron transfer.

After immobilization of the aptamer strands onto the modified AEs, a slight decrease in peak current and increase in ΔE_p value were found, which can be ascribed to the repulsion interaction between the negatively charged phosphate groups on aptamer strands and $[Fe(CN)_6]^{3-/4-}$ redox probe. As a result, the electron transfer at the electrode/electrolyte interface is hampered [55]. Here, Apt/$Ag/Ag_2O/Ag_2S/MoS_{2(800)}$/AE shows a small decrease in peak current, which indicates that only few aptamer strands were immobilized onto the modified AE surface. By contrast, Apt/Ag-PMo_{12}/AE has large variation in the peak current, which is due to the high bioaffinity of Apt/Ag-PMo_{12}/AE toward the aptamer, thus facilitating additional aptamer anchoring over the modified AE surface.

When the proposed aptasensors were used to detect BPA in water solution, their peak currents continuously decline, and accordingly, their ΔE_p values increase. As previously mentioned, the immobilized aptamer strands would combine with the BPA molecules to form the aptamer-BPA complex. This leads to the conformation change of aptamer strands [56], which can further disturb the electron transfer and decrease the peak current. Although the Ag-PMo_{12}-based aptasensor shows superior aptamer immobilization performance, the change of electrochemical signal by detecting BPA is smaller than that based on $Ag/Ag_2O/Ag_2S/MoS_{2(600)}$. This finding indicates that the formed aptamer-BPA complex would partially remove from the Ag-PMo_{12} matrix.

The consistent results were verified by EIS results using the series of Ag-PMo_{12}-derived nanohybrid-based aptasensors (Fig. 3) and the PMo_{12}- and Ag-PMo_{12}-based ones (Fig. S10). Table S1 summarizes the deduced charge transfer resistance (R_{ct}) values for each step during the fabrication of different aptasensors. The three aptasensors based on $Ag_2O/Ag_2S/MoS_2$ nanohybrids exhibit similar electrochemical behaviors (Fig. 3a–c). The bare AEs show small R_{ct} values of 30.9–33.9 Ω, verifying their remarkable electrochemical activity and making the electron transfer at the electrode/electrolyte feasible [55]. The modification with PMo_{12}, Ag-PMo_{12}, and the series of Ag-PMo_{12}-derived nanohybrids results in the larger R_{ct} values (from 165.7 Ω to 305.6 Ω) of the modified electrodes than the bare AEs. This finding suggests that the series of Ag-PMo_{12}-derived nanohybrids exhibit inferior electrochemical activities to the bare AEs, which hinders the electron transfer and increases the R_{ct} values. In comparison with the reported nanoporous frameworks (Table S2), such as Tb-MOF-on-Fe-MOF (529 Ω) [57], ZrHf-MOF (475 Ω) [58], Zr-MOF (523 Ω) [59], and CeCu-MOF (650 Ω) [60], the Ag-PMo_{12}-derived nanohybrids show better electrochemical performance, which can enlarge the detecting electrochemical signal and further facilitate the sensitivity of aptasensors. Among the three nanohybrids, Ag-$MoS_{2(300)}$ shows the smallest R_{ct} value (165.7 Ω), manifesting its excellent electrochemical performance. Under the lower temperature (300 °C), the Ag-PMo_{12} nanostructure was partially decomposed. Given the intrinsic high electrochemical activity of PMo_{12}, the Ag-PMo_{12} nanosheet has an opened electron transport channel, thereby providing additional electroactive sites, shorter electron transfer, and electrolyte diffusion pathways [61]. After the aptamers were anchored over the modified AEs, the R_{ct} values continuously increase (from 268.9 Ω to 788.9 Ω). When detecting BPA from aqueous solution, the EIS responses continuously raise and display even large R_{ct} values ranging from 526.5 Ω to 1101.3 Ω. However, the differences of these aptasensors are difficult to evaluate only using the R_{ct} values, caused by each modified step during the developing procedure for different sensors. Therefore, a proper analytical method must be explored to confirm the sensing performance and optimize the platform materials.

Normally, the differential of R_{ct} values (ΔR_{ct}) before and after the electrode modification with different layers for each step is correlated with the amount of added materials [44]. When the electrochemical biosensors exhibit excellent reproducibility, an increase in R_{ct} can be observed as a result of the targeted binding [55]. Therefore, the large ΔR_{ct} value obtained by detecting BPA indicates the excellent sensing performance of an aptasensor. The ΔR_{ct} values for each step against different aptasensors based on PMo_{12}, Ag-PMo_{12}, and Ag-PMo_{12}-derived nanohybrids were summarized in Fig. 3d and Table S3. Among the three types of Ag-PMo_{12}-derived nanohybrids, Ag-$MoS_{2(300)}$ leads to the smallest ΔR_{ct} value (134.8 Ω), revealing its good electrochemical activity. The other two nanohybrids show comparable ΔR_{ct} values of 189.1 and 209.8 Ω, respectively. After the immobilization of aptamer, $Ag/Ag_2O/Ag_2S/MoS_{2(600)}$/AE exhibits optimal immobilization ability, resulting in a ΔR_{ct} value of 212.4 Ω. As previously reported [41], Ag^0 mainly interact with the oxygen atoms of the phosphodiester bond and deoxyribose in DNA, while Ag^+ preferentially interact with the nitrogen atoms of DNA bases. This effect is much more significant when the Ag^+ ions are transferred to Ag_2O and Ag_2S. Therefore, different valence states of Ag facilitate the aptamer strands to largely anchor over the modified AE. On the contrary, $Ag/Ag_2O/Ag_2S/MoS_{2(800)}$/AE has poor aptamer anchoring, only showing a small ΔR_{ct} value of 66.1 Ω. The TEM and XRD results indicate that the crystallinity of $Ag/Ag_2O/Ag_2S/MoS_{2(800)}$ is the highest. The highly regular nanostructure is unfavorable for anchoring aptamer strands [62] because of its interior detection efficiency for BPA. The obtained ΔR_{ct} value of BPA/Apt/$Ag/Ag_2O/Ag_2S/MoS_{2(600)}$/AE is large (444.6 Ω) due to the specific adsorption of BPA with the aptamer immobilized onto the modified AE [63]. Consequently, $Ag/Ag_2O/Ag_2S/MoS_{2(600)}$ was chosen as the platform for developing the BPA aptasensor. This nanohybrid could not only improve the electron transfer but also increase the binding sites for aptamer strands, thus exhibiting superior sensing performance [55].

The optimal conditions for detecting BPA using the $Ag/Ag_2O/Ag_2S/MoS_{2(600)}$-based aptasensor were also evaluated (S4 in Supplementary Material): the $Ag/Ag_2O/Ag_2S/MoS_{2(600)}$ dispersion concentration is 1.0 mg mL^{-1}; the aptamer concentration is 100 nM; and the binding time for BPA is 40 min.

3.3. Sensitivity of the developed aptasensor based on $Ag/Ag_2O/Ag_2S/MoS_{2(600)}$ nanohybrid

The detection sensitivity, which can be represented by the limit of detection (LOD), should be determined for the aptasensor [55]. The low LOD suggests high sensitivity of the electrochemical aptasensor. The dynamic range of the developed $Ag/Ag_2O/Ag_2S/MoS_{2(600)}$-based aptasensor was separately tested by incubating with BPA solutions at concentrations ranging from 1 fg mL^{-1} to 1 pg mL^{-1}. Fig. 4a shows that the EIS responses for BPA detection increase with the increased BPA concentrations. The BPA solution with high concentration would lead to the formation of additional aptamer-BPA complexes, which greatly hinder the electron transfer at electrolyte/electrode interface [55]. The calibration curve could be achieved from the ΔR_{ct} values of five independent $Ag/Ag_2O/Ag_2S/MoS_{2(600)}$-based aptasensors (Fig. 4b). The obtained ΔR_{ct} values increase with increscent BPA concentration ranging from 1 fg·mL^{-1} to 1 pg mL^{-1}. However, these values slowly approach equilibrium when the BPA concentration is above 1 pg mL^{-1}. The ΔR_{ct} values were taken as the functions of the logarithm of BPA concentration. Accordingly, a good linear relationship (Fig. 4b inset), having a regression equation of ΔR_{ct} (Ω) = 647.46 + 172.44 log C_{BPA} with correlation coefficient R^2 = 0.9921, was obtained. The LOD was deduced to be 0.2 fg mL^{-1} with a signal to noise ratio of 3 according to the IUPAC approach [64].

The proposed electrochemical sensing platform based on the $Ag/Ag_2O/Ag_2S/MoS_{2(600)}$ nanohybrid shows a lower LOD and wider dynamic range, compared with the reported BPA aptasensors (Table 1). The promising sensing performances can be ascribed to the following factors: (i) the $Ag/Ag_2O/Ag_2S/MoS_{2(600)}$ nanohybrid exhibits some

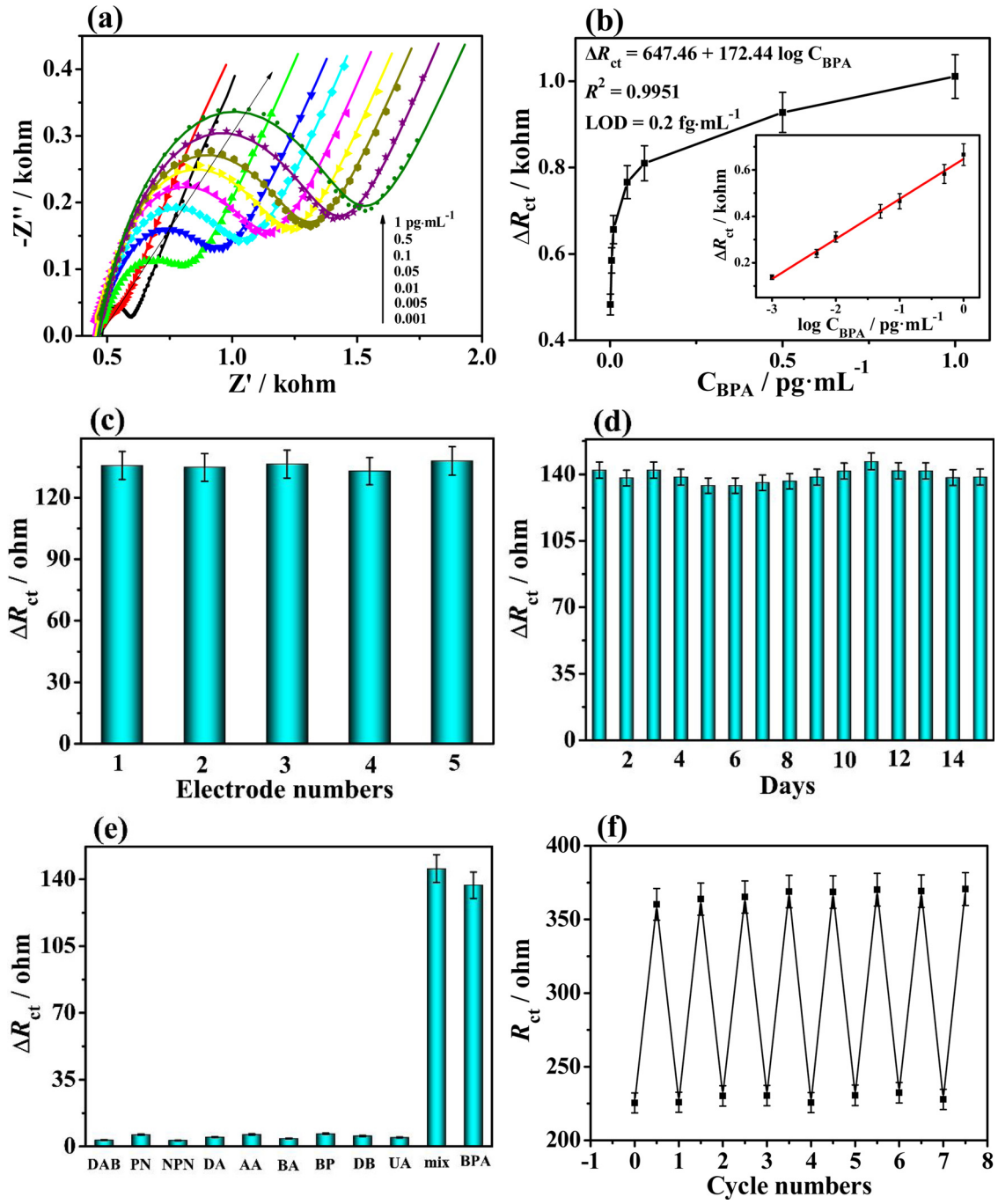

Fig. 4. (a) EIS Nyquist plots for detection of BPA at different concentrations (0.001, 0.005, 0.01, 0.05, 0.1, 0.5, and 1 pg mL^{-1}) using the Ag/Ag_2O/Ag_2S/$MoS_{2(600)}$-based aptasensor. (b) Calibration curves between ΔR_{ct} and BPA concentrations (inset: the linear fit plot of ΔR_{ct} as a function of the logarithm of BPA concentration, where the error bars are standard deviations for n = 3). (c) Reproducibility, (d) Stability, (e) Selectivity, and (f) Regenerability of the proposed aptasensor for BPA detection (n = 3).

intrinsic features, such as physiochemical stability and high electrochemical activity, thus providing high stability in the water solution, accelerating the electron transfer, and generating more sites for aptamer immobilization; (ii) the assembled 2D nanosheets of the POM-derived nanohybrid shows good adsorption ability, thus boosting the stability of aptamer-BPA complex and enhancing the sensing performance; and (iii) the superior electrochemical activity of the nanohybrid can avoid the use of electrode indicator along with the label-free design, thereby reducing the cost and shortening the fabrication procedure of aptasensors.

3.4. Reproducibility, stability, selectivity and regenerability of the Ag/Ag_2O/Ag_2S/$MoS_{2(600)}$-based aptasensor

Reproducibility of the Ag/Ag_2O/Ag_2S/$MoS_{2(600)}$-based aptasensor (Fig. 4c) was explored by repeating the measurements of five similarly modified AEs to detect BPA. The result shows that the relative standard derivation (RSD) is 4.4 %, suggesting the good reproducibility of aptasensor. The long-term stability of BPA/Apt/Ag/Ag_2O/Ag_2S/$MoS_{2(600)}$/AE was also investigated by storing at 4 °C in refrigerator for 15 days (Fig. 4d), which was then measured at the same BPA concentration level. The result shows that the change of ΔR_{ct} is 4.7 %,

Table 1
Comparison with the reported techniques for BPA detection.

Materials	Detection method	Detection range ($pg\,mL^{-1}$)	LOD ($pg\,mL^{-1}$)	Refs.
graphene-coated Ag nanoparticles on Si fibers	solid-phase micro-extraction-SERS	$2 \times 10^6 - 1 \times 10^8$	1×10^5	[66]
amino-functionalized magnetic Fe_3O_4 and AHN-labeled aptamer	fluorescence	200–8000	47	[7]
nafion/magnetic Fe_3O_4 nanocrystals	electrochemiluminescence	10–5000	0.66	[67]
Au-Pt@SiO_2 nanospheres	square wave voltammetry and differential pulse voltammetry	$1 \times 10^4 - 1 \times 10^7$	1800	[68]
gold nanoparticle-nanorod heteroassemblies	SERS	1–1000	3.9	[69]
monoclonal antibody	fluorescence polarization immunoassay	$1.13 \times 10^4 - 9.04 \times 10^5$	5600	[70]
$Ag/Ag_2O/Ag_2S/MoS_{2(600)}$	EIS	0.001–1	2×10^{-4}	This work

indicating the excellent stability of this aptasensor. High specificity is another important feature of the $Apt/Ag/Ag_2O/Ag_2S/MoS_{2(600)}/AE$ aptasensor. Herein, different types of interferences, including BPA analogs (BA, BP, DB, DAB, PN, and NPN) and small biomolecules (DA, AA, and UA), present in the biological fluid with 100-fold BPA concentration were used to test the specificity. The obtained ΔR_{ct} value caused by the pure BPA is set as 100 %. The ΔR_{ct} values in the solutions containing interferences have fluctuations in 2.3 %–4.8 %, confirming the high selectivity of this aptasensor (Fig. 4e). When all the interferences are mixed with BPA, the obtained ΔR_{ct} value is only 106.28 % compared to that of pure BPA. In contrast with most conventional aptasensors for BPA, the present sensor can also be well regenerated. Fig. 4f illustrates a slight fluctuation in ΔR_{ct} values of the proposed aptasensor during seven regeneration runs for detection of BPA, suggesting its good regenerability. This is because, in the presence of BPA, due to the specific recognition of aptamer toward BPA, the aptamer strands immobilized on the modified electrode surface partially folded to form the aptamer-BPA complex [63]. This would result in the positive change of electrochemical responses. Sodium hydroxide has strong causticity, after soaking the BPA-bonded electrode (BPA/Apt/Material/AE) with sodium hydroxide, the aptamer strands deactivated temporarily and changed their configuration into linear shape [65]. Therefore, the BPA released from the aptamer-BPA complex, leading to the Apt/Material/AE retained. It further resulted in another negative change of the electrochemical responses. After rinsing the electrode thoroughly by PBS, the Apt/Material/AE was used to bond with BPA once again and realized the sensitive detection. The treatment of soaking in sodium hydroxide and then rinsing with PBS will obtain a complete cycle of regeneration test.

3.5. Real sample analysis

Considering the excellent biosensing performance of the $Ag/Ag_2O/Ag_2S/MoS_{2(600)}$-based aptasensor, it was further applied to detect BPA in real samples, such as river water, milk, and human serum, to assess the applicability. The aforementioned real samples were pretreated prior to use. Afterwards, these samples were spiked with BPA solutions at different concentrations and examined using the developed aptasensor. The BPA concentrations in different samples were calculated and listed in Tables S4–S6 according to the calibration curve (Fig. 4b inset) and the deduced equation. In comparison to the theoretical values, the deduced BPA concentrations show recoveries of 96.8–108.7 %, 98.9–109.6 % and 96.3–109.6 % and RSDs of 0.2–1.1 %, 0.3–1.3 % and 0.3–0.9 % for river water, milk and human serum samples, respectively. These results definitely indicate that the aptasensor shows good applicability and can be used to detect trace BPA in real samples.

4. Conclusions

In conclusion, a novel 2D bimetallic AgMo heteronanostructure composed of multicomponent Ag, Ag_2O, Ag_2S, and MoS_2 has been synthesized, which can be well applied to immobilize BPA aptamer and further fabricate aptasensor for trace BPA detection in water solution. The prepared AgMo nanohybrid inherits the intrinsic features of Ag-PMo_{12}, such as skeleton structure, physiochemical stability, and electrochemical activity. In comparison, the optimized $Ag/Ag_2O/Ag_2S/MoS_{2(600)}$ nanohybrid shows high stability in water solution, fast electron transfer, and more sites for aptamer immobilization. As a result, the $Ag/Ag_2O/Ag_2S/MoS_{2(600)}$-based aptasensor shows superior sensing performance with an extremely low LOD of $0.2\,fg\,mL^{-1}$ and a wide linear BPA concentration from $1\,fg\,mL^{-1}$ to $1\,pg\,mL^{-1}$. This proposed sensing strategy exhibits clear advantages, namely, feasible preparation of the electrode materials, label-free aptamer strands, and nonuse of electrochemical indicators. We believe that this new strategy is of great potentials for convenient detection of harmful residues in environment and food.

CRediT authorship contribution statement

Yingpan Song: Investigation, Formal analysis, Writing - original draft. **Miaoran Xu:** Data curation, Writing - review & editing. **Zhenzhen Li:** Methodology, Writing - review & editing. **Lina He:** Data curation, Writing - review & editing. **Mengyao Hu:** Methodology, Writing - review & editing. **Linghao He:** Supervision, Writing - review & editing. **Zhihong Zhang:** Visualization, Writing - review & editing, Funding acquisition. **Miao Du:** Supervision, Project administration, Writing - review & editing.

Declaration of Competing Interest

The authors declare that they have no conflict of interest.

Acknowledgements

This work was supported by the National Natural Science Foundation of China (U1604127) and the Key Research Project of University of Henan Province (19zx004).

Appendix A. Supplementary data

Supplementary material related to this article can be found, in the online version, at doi:https://doi.org/10.1016/j.snb.2020.128527.

References

[1] R. Valentino, V.D. Esposito, F. Ariemma, I. Cimmino, F. Beguinot, P. Formisano, Bisphenol A environmental exposure and the detrimental effects on human metabolic health: is it necessary to revise the risk assessment in vulnerable population? J. Endocrinol. Invest. 39 (2016) 259–263.
[2] P. Deb, A. Bhan, I. Hussain, K.I. Ansari, S.A. Bobzean, T.K. Pandita, L.I. Perrotti, S.S. Mandal, Endocrine disrupting chemical, bisphenol-A, induces breast cancer associated gene HOXB9 expression in vitro and in vivo, Gene 590 (2016) 234–243.
[3] C. Peng, N. Pan, Z. Xie, L. Liu, J. Xiang, C. Liu, Determination of bisphenol A by a gold nanoflower enhanced Enzyme-Linked immunosorbent assay, Anal. Lett. 49

(2016) 1492–1501.
[4] L. Lin, L.A. Stanciu, Bisphenol A detection using gold nanostars in a SERS improved lateral flow immunochromatographic assay, Sens. Actuators B-Chem. 276 (2018) 222–229.
[5] Z. Luo, J. Zhang, Y. Wang, J. Chen, Y. Li, Y. Duan, An aptamer based method for small molecules detection through monitoring salt-induced AuNPs aggregation and surface plasmon resonance (SPR) detection, Sens. Actuators B-Chem. 236 (2016) 474–479.
[6] K. Matsumoto, B.D.B. Tiu, A. Kawamura, R.C. Advincula, T. Miyata, QCM sensing of bisphenol A using molecularly imprinted hydrogel/conducting polymer matrix, Polym. J. 48 (2016) 525–532.
[7] M. Li, L. Hu, C. Niu, D. Huang, G. Zeng, A magnetic separation fluorescent aptasensor for highly sensitive detection of bisphenol A, Sens. Actuators B-Chem. 266 (2018) 805–811.
[8] S. Rajabnejad, H. Badibostan, A. Verdian, G.R. Karimi, E. Fooladi, J. Feizy, Aptasensors as promising new tools in bisphenol A detection - an invisible pollution in food and environment, Microchem. J. 155 (2020) 104722.
[9] R. Zhang, Y. Zhang, X. Deng, S. Sun, Y. Li, A novel dual-signal electrochemical sensor for bisphenol A determination by coupling nanoporous gold leaf and self-assembled cyclodextrin, Electrochim. Acta 271 (2018) 417–424.
[10] K. Kamil Reza, M. Azahar Ali, M.K. Singh, V.V. Agrawal, A.M. Biradar, Amperometric enzymatic determination of bisphenol A using an ITO electrode modified with reduced graphene oxide and Mn_3O_4 nanoparticles in a chitosan matrix, Microchim. Acta 184 (2017) 1809–1816.
[11] X. Wang, S. Reisberg, N. Serradji, G. Anquetin, M.C. Pham, W. Wu, C.Z. Dong, B. Piro, E-assay concept: detection of bisphenol A with a label-free electrochemical competitive immunoassay, Biosens. Bioelectron. 53 (2014) 214–219.
[12] Z. Yu, Y. Luan, H. Li, W. Wang, X. Wang, Q. Zhang, A disposable electrochemical aptasensor using single-stranded DNA–methylene blue complex as signal-amplification platform for sensitive sensing of bisphenol A, Sens. Actuators B-Chem. 284 (2019) 73–80.
[13] G. Maduraiveeran, M. Sasidharan, V. Ganesan, Electrochemical sensor and biosensor platforms based on advanced nanomaterials for biological and biomedical applications, Biosens. Bioelectron. 103 (2018) 113–129.
[14] H. Hu, A. Zavabeti, H. Quan, W. Zhu, H. Wei, D. Chen, J.Z. Ou, Recent advances in two-dimensional transition metal dichalcogenides for biological sensing, Biosens. Bioelectron. 142 (2019) 111573.
[15] C. Liu, A. Tuffour, J. Liao, M. Li, Q. Lv, D. Zhou, L. Gao, Highly sensitive detection of Hg^{2+} using molybdenum disulfide-DNA sensors, Chem. Phys. 534 (2020) 110758.
[16] Y. Shu, L. Zhang, H. Cai, Y. Yang, J. Zeng, D. Ma, Q. Gao, Hierarchical Mo_2C@MoS_2 nanorods as electrochemical sensors for highly sensitive detection of hydrogen peroxide and cancer cells, Sens. Actuators B-Chem. 311 (2020) 127863.
[17] L. Liu, S. Zhu, Y. Wei, X. Liu, S. Jiao, J. Yang, Ultrasensitive detection of miRNA-155 based on controlled fabrication of AuNPs@MoS_2 nanostructures by atomic layer deposition, Biosens. Bioelectron. 144 (2019) 111660.
[18] H. Park, S.R. Dugasani, D. Kang, J. Jeon, S.K. Jang, S. Lee, Y. Roh, S.H. Park, J. Park, N- and p-type doping phenomenon by artificial DNA and M-DNA on two-dimensional transition metal dichalcogenides, ACS Nano 8 (2014) 11603–11613.
[19] J. Feng, K. Liu, M. Graf, M. Lihter, R.D. Bulushev, D. Dumcenco, D.T.L. Alexander, D. Krasnozhon, T. Vuletic, A. Kis, A. Radenovic, Electrochemical reaction in single layer MoS_2: nanopores opened atom by atom, Nano Lett. 15 (2015) 3431–3438.
[20] P. Zuo, L. Jiang, X. Li, B. Li, P. Ran, X. Li, L. Qu, Y. Lu, Metal (Ag, Pt)-MoS_2 hybrids greenly prepared through photochemical reduction of femtosecond laser pulses for SERS and HER, ACS Sustain. Chem. Eng. 6 (2018) 7704–7714.
[21] Y. Zhao, G. Deng, X. Liu, L. Sun, H. Li, Q. Cheng, K. Xi, D. Xu, MoS_2/Ag nanohybrid: a novel matrix with synergistic effect for small molecule drugs analysis by negative-ion matrix-assisted laser desorption/ionization time-of-flight mass spectrometry, Anal. Chim. Acta 937 (2016) 87–95.
[22] G. Oudeng, M. Au, J. Shi, C. Wen, M. Yang, One-step in situ detection of miRNA-21 expression in single cancer cells based on biofunctionalized MoS_2 nanosheets, ACS Appl. Mater. Inter. 10 (2017) 350–360.
[23] J. Liu, X. Chen, Q. Wang, M. Xiao, D. Zhong, W. Sun, G. Zhang, Z. Zhang, Ultrasensitive monolayer MoS_2 field-Effect transistor based DNA sensors for screening of down syndrome, Nano Lett. 19 (2019) 1437–1444.
[24] A.B. Laursen, S. Kegnaes, S. Dahl, I. Chorkendorff, Molybdenum sulfides-efficient and viable materials for electro - and photoelectrocatalytic hydrogen evolution, Energy Environ. Sci. 5 (2012) 5577–5591.
[25] Z. Zhang, K. Chen, Q. Zhao, M. Huang, X. Ouyang, Effects of noble metal doping on hydrogen sensing performances of monolayer MoS_2, Mater. Res. Express 7 (2020) 015501.
[26] Q. Fang, X. Zhao, Y. Huang, K. Xu, T. Min, F. Ma, Junction-configuration-dependent interfacial electronic states of a monolayer MoS_2/metal contact, J. Mater. Chem. C 7 (2019) 3607–3616.
[27] H. Yan, Y. Xie, Y. Jiao, A. Wu, C. Tian, X. Zhang, L. Wang, H. Fu, Holey reduced graphene oxide coupled with an Mo_2N-Mo_2C heterojunction for efficient hydrogen evolution, Adv. Mater. 30 (2018) 1704156.
[28] L. Zhang, T. Mi, M.A. Ziaee, L. Liang, R. Wang, Hollow POM@MOF hybrid-derived porous Co_3O_4/$CoMoO_4$ nanocages for enhanced electrocatalytic water oxidation, J. Mater. Chem. A 6 (2018) 1639–1647.
[29] J. Hou, B. Zhang, Z. Li, S. Cao, Y. Sun, Y. Wu, Z. Gao, L. Sun, Vertically aligned oxygenated-CoS_2-MoS_2 heteronanosheet architecture from polyoxometalate for efficient and stable overall water splitting, ACS Catal. 8 (2018) 4612–4621.
[30] R. Breitwieser, A. Garnier, T. Auvray, A. Ngo, B. Baptiste, N. Menguy, A. Proust, C. Petit, F. Volatron, C. Salzemann, Protective effect of polyoxometalates in {Mo_{132}}/maghemite binary superlattices under annealing, Front. Chem. 7 (2019) 830.
[31] J.C. Ye, J.J. Chen, R.M. Yuan, D.R. Deng, M.S. Zheng, L. Cronin, Q.F. Dong, Strategies to explore and develop reversible redox reactions of Li-S in electrode architectures using silver-polyoxometalate clusters, J. Am. Chem. Soc. 140 (2018) 3134–3138.
[32] B. Wang, M. Zhao, M. Mehdi, G. Wang, P. Gao, K. Zhang, Biomolecule-assisted synthesis and functionality of metal nanoclusters for biological sensing: a review, Mater. Chem. Front. 3 (2019) 1722–1735.
[33] H. Zhang, X. Xu, H. Lin, M.A.U. Din, H. Wang, X. Wang, Silver nanocrystal-decorated polyoxometalate single-walled nanotubes as nanoreactors for desulfurization catalysis at room temperature, Nanoscale 9 (2017) 13334–13340.
[34] S. Zhan, C. Li, H. Tian, C. Ma, H. Liu, J. Luo, M. Li, Synthesis, characterization and dye removal behavior of core-shell-shell Fe_3O_4/Ag/polyoxometalates ternary nanocomposites, Nanomaterials 9 (2019, 1255).
[35] M. Dou, X. Huang, G. Yang, Two inorganic-organic hybrid silver-polyoxometalates as reusable catalysts for one-pot synthesis of propargylamines via a three-component coupling reaction at room temperature, CrystEngComm 22 (2020) 2642–2648.
[36] S. Guo, F. Li, L. Chen, D.R. Macfarlane, J. Zhang, Polyoxometalate-Promoted electrocatalytic CO_2 reduction at nanostructured silver in dimethylformamide, ACS Appl. Mater. Inter. 10 (2018) 12690–12697.
[37] X. Zhao, L. Gong, C. Wang, C. Wang, K. Yu, B. Zhou, A facile grinding method for the synthesis of 3D Ag metal–organic frameworks (MOFs) containing $Ag_6Mo_7O_{24}$ for high-performance supercapacitors, Chem. Eur. J. 26 (2020) 4613–4619.
[38] X. Yan, S. Li, J. Bao, N. Zhang, B. Fan, R. Li, X. Liu, Y. Pan, Immobilization of highly dispersed ag nanoparticles on carbon nanotubes using electron-assisted reduction for antibacterial performance, ACS Appl. Mater. Inter. 8 (2016) 17060–17067.
[39] L. Zhao, D. Kong, Z. Wu, G. Liu, Y. Gao, X. Yan, F. Liu, X. Liu, C. Wang, J. Cui, G. Lu, Interface interaction of MoS_2 nanosheets with DNA based aptameric biosensor for carbohydrate antigen 15-3 detection, Microchem. J. 155 (2020) 104675.
[40] F. Liu, Y. Zhang, H. Wang, L. Li, W. Zhao, J. Shen, L. Liang, Study on the adsorption orientation of DNA on two-dimensional MoS_2 surface via molecular dynamics simulation: a vertical orientation phenomenon, Chem. Phys. 529 (2020) 110546.
[41] I.L. Volkov, A. Smirnova, A.A. Makarova, Z.V. Reveguk, R.R. Ramazanov, D.Y. Usachov, V.K. Adamchuk, A.I. Kononov, DNA with ionic, atomic, and clustered silver: an XPS study, J. Phys. Chem. B 121 (2017) 2400–2406.
[42] L. Zhou, D. Jiang, X. Du, D. Chen, J. Qian, Q. Liu, N. Hao, K. Wang, Femtomolar sensitivity of bisphenol A photoelectrochemical aptasensor induced by visible light-driven TiO_2 nanoparticle-decorated nitrogen-doped graphene, J. Mater. Chem. B 4 (2016) 6249–6257.
[43] Z.S. Pehlivan, M. Torabfam, H. Kurt, C. Ow-Yang, N. Hildebrandt, M. Yüce, Aptamer and nanomaterial based FRET biosensors: a review on recent advances, Microchim. Acta 186 (2019) 563.
[44] Y. Song, F. Duan, S. Zhang, J. Tian, Z. Zhang, Z. Wang, C. Liu, W. Xu, M. Du, Iron oxide@mesoporous carbon architectures derived from an Fe(II)-based metal organic framework for highly sensitive oxytetracycline determination, J. Mater. Chem. A 5 (2017) 19378–19389.
[45] X. Shi, M. Fujitsuka, S. Kim, T. Majima, Faster electron injection and more active sites for efficient photocatalytic h_2 evolution in g-C_3N_4/MoS_2 hybrid, Small 14 (2018) 1703277.
[46] J. Wei, Y. Lei, H. Jia, J. Cheng, H. Hou, Z. Zheng, Controlled in situ fabrication of Ag_2O/AgO thin films by a dry chemical route at room temperature for hybrid solar cells, Dalton Trans. 43 (2014) 11333–11338.
[47] F. Wang, H. Yang, Y. Zhang, Enhanced photocatalytic performance of $CuBi_2O_4$ particles decorated with Ag nanowires, Mater. Sci. Semicon. Proc. 73 (2018) 58–66.
[48] J. Xie, J. Zhang, S. Li, F. Grote, X. Zhang, H. Zhang, R. Wang, Y. Lei, B. Pan, Y. Xie, Controllable disorder engineering in oxygen-incorporated MoS_2 ultrathin nanosheets for efficient hydrogen evolution, J. Am. Chem. Soc. 135 (2013) 17881–17888.
[49] Y. Ge, W. Shen, X. Wang, H. Feng, L. Feng, Synthesis and bactericidal action of Fe_3O_4/AgO bifunctional magnetic-bactericidal nanocomposite, Colloid Surf. A 563 (2019) 160–169.
[50] M.J. Height, S.E. Pratsinis, O. Mekasuwandumrong, P. Praserthdam, Ag-ZnO catalysts for UV-photodegradation of methylene blue, Appl. Catal. B-Environ. 63 (2006) 305–312.
[51] J. Zhou, H. Xiao, B. Zhou, F. Huang, S. Zhou, W. Xiao, D. Wang, Hierarchical MoS_2–rGO nanosheets with high MoS_2 loading with enhanced electro-catalytic performance, Appl. Surf. Sci. 358 (2015) 152–158.
[52] A. Pendashteh, J. Palma, M. Anderson, R. Marcilla, $NiCoMnO_4$ nanoparticles on N-doped graphene: highly efficient bifunctional electrocatalyst for oxygen reduction/evolution reactions, Appl. Catal. B-Environ. 201 (2017) 241–252.
[53] M. Usman, M. Arshad, S.S. Suvanam, A. Hallén, Influence of annealing environment on the ALD-Al_2O_3/4H-SiC interface, J. Phys. D Appl. Phys. 51 (2018) 105111.
[54] Y. Liu, H. Ma, J. Gao, D. Wu, X. Ren, T. Yan, X. Pang, Q. Wei, Ultrasensitive electrochemical immunosensor for SCCA detection based on ternary Pt/PdCu nanocube anchored on three-dimensional graphene framework for signal amplification, Biosens. Bioelectron. 79 (2016) 71–78.
[55] N. Zhou, F. Su, Z. Li, X. Yan, C. Zhang, B. Hu, L. He, M. Wang, Z. Zhang, Gold nanoparticles conjugated to bimetallic manganese(II) and iron(II) Prussian Blue analogues for aptamer-based impedimetric determination of the human epidermal growth factor receptor-2 and living MCF-7 cells, Microchim. Acta 186 (2019) 75.
[56] L. Kashefi-Kheyrabadi, J. Kim, H. Gwak, K. Hyun, N.H. Bae, S.J. Lee, H. Jung, A microfluidic electrochemical aptasensor for enrichment and detection of bisphenol A, Biosens. Bioelectron. 117 (2018) 457–463.
[57] M. Wang, M. Hu, Z. Li, L. He, Y. Song, Q. Jia, Z. Zhang, M. Du, Construction of Tb-MOF-on-Fe-MOF conjugate as a novel platform for ultrasensitive detection of carbohydrate antigen 125 and living cancer cells, Biosens. Bioelectron. 142 (2019)

111536.
[58] C. Gu, C. Guo, Z. Li, M. Wang, N. Zhou, L. He, Z. Zhang, M. Du, Bimetallic ZrHf-based metal-organic framework embedded with carbon dots: ultra-sensitive platform for early diagnosis of HER2 and HER2-overexpressed living cancer cells, Biosens. Bioelectron. 134 (2019) 8–15.
[59] L. He, F. Duan, Y. Song, C. Guo, S. Fang, 2D zirconium-based metal-organic framework nanosheets for highly sensitive detection of mucin 1: consistency between electrochemical and surface plasmon resonance methods, 2D Mater. 4 (2017) 025098.
[60] S. Wang, Z. Li, F. Duan, B. Hu, L. He, M. Wang, N. Zhou, Q. Jia, Z. Zhang, Bimetallic cerium/copper organic framework-derived cerium and copper oxides embedded by mesoporous carbon: label-free aptasensor for ultrasensitive tobramycin detection, Anal. Chim. Acta 1047 (2019) 150–162.
[61] M. Huang, P. Wang, Y. Liu, J. Zhao, Q. Lin, M. Lu, One-step synthesis of honeycomb-like Ni/Mn-PMo_{12} ultra-thin nanosheets for high-performance asymmetric supercapacitors, Appl. Surf. Sci. 497 (2019) 143760.
[62] S. Zhang, R. Geryak, J. Geldmeier, S. Kim, V.V. Tsukruk, Synthesis, assembly, and applications of hybrid nanostructures for biosensing, Chem. Rev. 117 (2017) 12942–13038.
[63] Y. Su, H. Xu, Y. Chen, J. Qi, X. Zhou, R. Ge, Z. Lin, Real-time and label-free detection of bisphenol A by an ssDNA aptamer sensor combined with dual polarization interferometry, New J. Chem. 42 (2018) 2850–2856.
[64] L. He, Z. Li, C. Guo, B. Hu, M. Wang, Z. Zhang, M. Du, Bifunctional bioplatform based on NiCo Prussian blue analogue: label-free impedimetric aptasensor for the early detection of carcino-embryonic antigen and living cancer cells, Sens. Actuators B-Chem. 298 (2019) 126852.
[65] X. Liu, J. Ren, L. Su, X. Gao, Y. Tang, T. Ma, L. Zhu, J. Li, Novel hybrid probe based on double recognition of aptamer-molecularly imprinted polymer grafted on up-conversion nanoparticles for enrofloxacin sensing, Biosens. Bioelectron. 87 (2017) 203–208.
[66] L. Qiu, Q. Liu, X. Zeng, Q. Liu, X. Hou, Y. Tian, L. Wu, Sensitive detection of bisphenol A by coupling solid phase microextraction based on monolayer graphene-coated Ag nanoparticles on Si fibers to surface enhanced Raman spectroscopy, Talanta 187 (2018) 13–18.
[67] J. Chai, X. Yu, J. Zhao, A. Sun, X. Shi, D. Li, An electrochemiluminescence sensor based on nafion/magnetic Fe_3O_4 nanocrystals modified electrode for the determination of bisphenol A in environmental water samples, Sens. Basel 18 (2018) 2537.
[68] L. Wu, H. Yan, J. Wang, G. Liu, W. Xie, Tyrosinase incorporated with Au-Pt@SiO_2 nanospheres for electrochemical detection of bisphenol A, J. Electrochem. Soc. 166 (2019) 562–568.
[69] J. Feng, L. Xu, G. Cui, X. Wu, W. Ma, H. Kuang, C. Xu, Building SERS-active heteroassemblies for ultrasensitive Bisphenol A detection, Biosens. Bioelectron. 81 (2016) 138–142.
[70] P. Huang, S. Zhao, S.A. Eremin, S. Zheng, D. Lai, Y. Chen, B. Guo, A fluorescence polarization immunoassay method for detection of the bisphenol A residue in environmental water samples based on a monoclonal antibody and 4'-(aminomethyl) fluorescein, Anal. Methods-UK 7 (2015) 4246–4251.

Yingpan Song is a lecturer in College of Material and Chemical Engineering, Zhengzhou University of Light Industry. She obtained her Ph. D. from Fuzhou University in 2016. Her research interests are advanced functional materials and biosensors.

Miaoran Xu is a graduate student at Zhengzhou University of Light Industry. Her research interests are metal-organic frameworks and biosensors.

Zhenzhen Li is a graduate student at Zhengzhou University of Light Industry. Her research interests are biomaterials and biomedical engineering.

Lina He is a graduate student at Zhengzhou University of Light Industry. Her research interests are nanocomposites and biosensors.

Mengyao Hu is a graduate student at Zhengzhou University of Light Industry. Her research interests are biomaterials and biosensors.

Linghao He is an associate professor in College of Material and Chemical Engineering, Zhengzhou University of Light Industry. She obtained her Ph. D. from Zhengzhou University in 2011. Her research interests are functional polymer materials and nanocomposites.

Zhihong Zhang is a professor in College of Material and Chemical Engineering, Zhengzhou University of Light Industry. She obtained her bachelor degree from Zhengzhou University and completed her doctoral work at Max-Plank Institute. After two years of postdoctoral work at National University of Singapore, she joined Zhengzhou University of Light Industry in 2005, since then she worked on bio-functional materials and biosensors.

Miao Du is a professor in College of Material and Chemical Engineering, Zhengzhou University of Light Industry. He obtained his Ph. D. from Nankai University in 2003 under the supervision of Prof. Xian-He Bu. He has worked with Prof. Thomas C. W. Mak at the Chinese University of Hong Kong and Dr Qiang Xu at the National Institute of Advanced Industrial Science and Technology of Japan. His research interests include coordination chemistry, crystal engineering, porous materials, biomaterials and biosensors.